13th International Symposium on Particle Image Velocimetry – ISPIV 2019
Munich, Germany, July 22-24, 2019

Uncertainty Reduction of FlowFit Flow Field Estimation by Use of Virtual Particles

Frithjof Ehlers*, Andreas Schröder, Sebastian Gesemann

German Aerospace Center (DLR), Institute of Aerodynamics and Flow Technology, Department of Experimental Methods, Germany

* frithjof.ehlers@dlr.de

Abstract

Flowfield measurements are nowadays performed with highspeed camera recordings of tracer particles in an illuminated fluid layer or volume. The following post-processing is key to the quality of the resulting velocity and/or acceleration fields. Dense 3D particle tracking following the Shake-The-Box method (Schanz et al., 2016) yields accurate but scattered data. Sophisticated interpolation schemes were proposed that can make use of further physical constraints from the Navier-Stokes equations in order to simultaneously determine velocity and acceleration fields as solutions to an inverse problem. This allows to resolve structures beyond the classical Nyquist limit for each single field variable. So far, the full temporal domain has either not been considered yet (Gesemann et al., 2016) or the temporal coupling of several time instants via simulation methods resulted in high computational costs (Schneiders and Scarano, 2018). This work shows that the introduction of memory to the reconstruction process (by temporal coupling) results in improved flow field reconstructions. For this purpose, additional artificial Lagrangian tracers (virtual particles) were advected between the fields, which is the most natural way to achieve temporal coupling in the framework of such algorithms. Several contributions like reconstruction error correlations and the flow field regularization within the inverse problem were revised to explain the improvements.

1 Introduction

From experiments, data is available in the form of particle pictures from which particle tracks can be inferred by tracking techniques such as tomographic PTV (Schröder et al., 2011) or Shake-The-Box (Schanz et al., 2016). But complete knowledge of the velocity field is sought on the basis of the scattered velocity and acceleration data. For this purpose different spatial interpolation algorithms were proposed, such as FlowFit (Gesemann et al., 2016) and VIC+ (Schneiders et al., 2015), which take Lagrangian particle track data (position, velocity and acceleration) as input and exploit known physical properties such as continuity and the Navier-Stokes equations for incompressible and uniform-density flows to reconstruct accurate and high resolution velocity, acceleration and pressure fields. The mentioned algorithms reach higher spatial resolutions beyond Nyquist than interpolation schemes that make use of the constraint of solenoidality only, due to the increased amount of data.

These algorithms reconstruct single time instants, i.e. they take particle clouds at a certain time and try to fill up the missing spatial information by solving an inverse non-linear optimization problem with physical constraints. However, there is still potential for further increase of precision by combining the information from subsequent time instants, since the current procedure does not a priori impose temporal consistency. This might cause unnatural behaviour to occur because the fields of interest are almost always undersampled, e.g. due to limited particle seeding or high Reynolds numbers. If particles randomly occur close to a structure, i.e. a region with high velocity gradient tensor, it will be reconstructed with higher accuracy than in a case with a more anfavourable particle distribution, even if the structure itself is persistent over time.

More recently Schneiders and Scarano (2018) proposed a method called *time-segment-assimilation* (TSA) that incorporates multiple time steps into the inverse problem of the flow field reconstruction by the vortex-in-cell time integration method (Christiansen, 1973). It performed well in recovering additional structures. This, however, is computationally very expensive due to the iterative nature of the algorithm. Instead, we aim to develope a method in which virtual particles from previous reconstructions are advected

into the following interpolation timestep with an individual weight dependend on (i) the Lagrangian correlation functions known from the track data and (ii) the local velocity gradient tensor as estimated. Usually, the time steps are about the size of the Kolmogorov time scale so the Lagrangian velocities and accelerations at two subsequent time instants are still significantly correlated. Therefore, a straightforward approach to combine the information of multiple reconstructions is to involve additional virtual particles into the reconstruction process that are advected with the estimated velocity and acceleration in order to act as information carrier between the reconstructed fields, thus enforcing consistency in time.

2 Virtual Experiments

Table 1: Information on the virtual experiments. T_c denotes the decorrelation time of acceleration.

	FIT				CF		
subdomain	$[0,\pi/8]\times[0,\pi/8]\times[0,\pi/8]$				$[-0.5,0.78]\times[0.64,0.96]\times[0,0.32]$		
frame spacing Δt	$0.01\approx\tau_\eta/4\approx T_c/8$				$0.04\approx T_c(y^+=40)/4$		
#particles	1600	6500	13000	26000	2000	8400	16400
average particle spacing	12η	7.52η	5.96η	4.73η	$40.3y^+$	$24.97y^+$	$19.98y^+$

Virtual experiments on two testcases of the Johns Hopkins Turbulence Database were performed. Cuboid subvolumes were chosen in the forced isotropic turbulence (FIT) dataset (Li et al., 2008) and the channel flow (CF) dataset (Graham et al., 2016). The latter is comoving in streamwise x-direction with a speed of 0.7 in order to keep track of the same flow structures over a greater range of time. The position and extent of the subdomains is documented in table 1. Several sets of particle tracks with different seeding densities were generated by making use of the database functions (Yu et al., 2012). To achieve homogeneous seeding, the subvolumes were extended by a buffer volume and, therein, random positions were drawn from a uniform probability density. All of these particles are integrated forward in time. At each time step, the particles inside the subvolumes are saved and utilized to generate the track-files, whereas the particles in the buffer layer get replaced by newly drawn random positions to guarantee a constant particle inflow into the subdomain. The velocities and accelerations in the trackfiles were determined from velocity and pressure by the provided spatio-temporal interpolation schemes (8th- and/or 4th-order Lagrange Polynomials and 4th-order centered finite differencing in space and Piecewise Cubic Hermite Interpolation Polynomials in time).

The frame spacing Δt, i.e. the size of the time step between successive reconstructions, was chosen rather conservative to enable variations in hindsight. The frame spacing in FIT was adjusted to approximately $\tau_\eta/4$, which corresponds to roughly 1/8 or 1/9 acceleration decorrelation times. The frame spacing in CF was chosen to be approximately 1/4 of the acceleration decorrelation time in the layer closest to the wall, i.e. the layer of the subdomain with the smallest dynamic timescale.

2.1 FlowFit Error Quantification

The FIT reconstruction was performed over the whole length of the dataset together with an exhaustive uncertainty analysis in order to develope criteria for error quantification and to obtain possible rules for an optimal seeding of virtual particles. For this purpose, the reconstruction error of velocities and accelerations in dependence of two criteria was evaluated. Therefor, the continuous B-spline interpolator of the reconstruction is sampled on the DNS grid and compared to the true field values. As a first criterion serves the distance to the nearest real particle d at which the velocity and acceleration was known. For the second criterion s, the unit vectors to the three nearest neighboured particles are summed up and the absolute value is taken. The resulting number will be close to zero if the nearest neighbours are distributed homogeneously around the gridpoint and greater zero otherwise. The reconstructed flow field might show an increased quality of spatial derivatives in regions of low s. Both criteria are illustrated in figure 1(a).

Interestingly, the error does not scale with the s-criterion but solely with nearest neighbour distance d. Here, a roughly linear dependence of the mean absolute velocity error on d is found for all seeding densities, see figure 2(b). The acceleration error behaves similarly. At the same time, the spectral signal-to-noise ratio (SNR) averaged over spatial components and time shows that a considerable amount of scales beyond the Nyquist limit is recovered by FlowFit, see figure 2(a). Eventually, one cannot deduce an optimal seeding

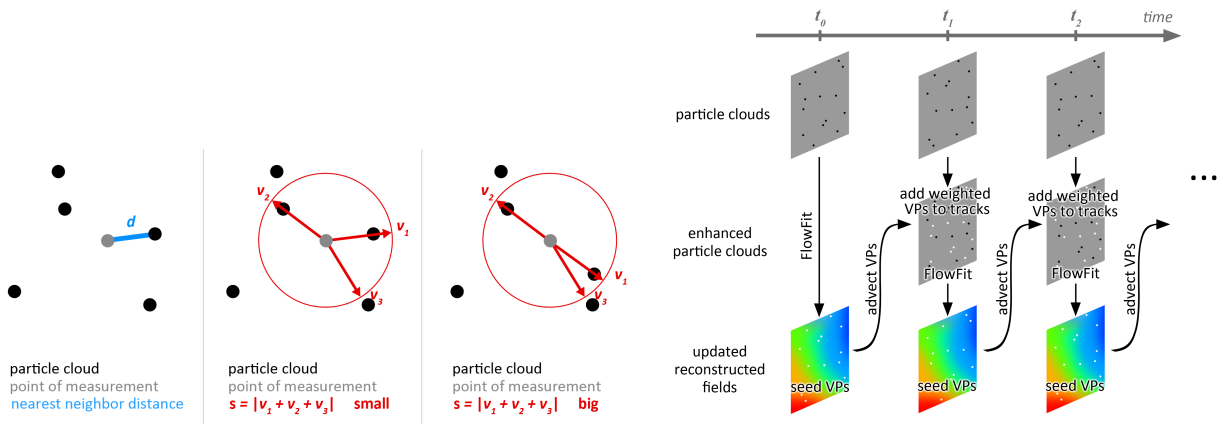

(a) Reconstruction errors where binned for both criteria, namely nearest neighbour distance d and uniformity of the neighbour distribution s.

(b) Outline of the iterative algorithm for temporal coupling of the single reconstructions by use of virtual particles (VPs). The initial particle clouds (black) are enhanced by the velocity data at the advected VP positions (white).

Figure 1: **(a)** Criteria for reconstruction error quantification based on particle cloud properties and **(b)** VP seeding strategy.

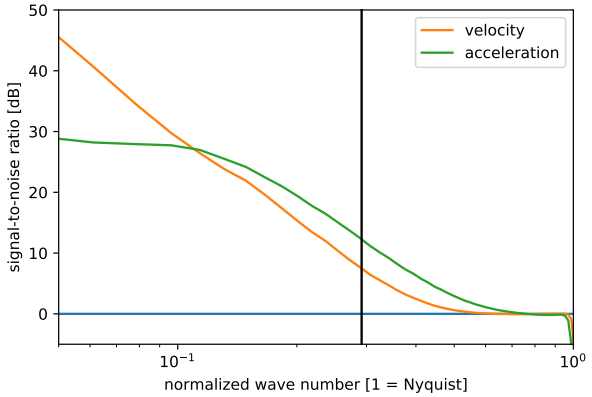

(a) Averaged spectral signal-to-noise ratio for velocity and acceleration in the FIT testcase with an average particle number of 6500 (spacing of 7.5 η). The wave numbers are normalized to the Nyquist wave number of the DNS grid. The Nyquist wave number concerning the average particle spacing is marked by the black line.

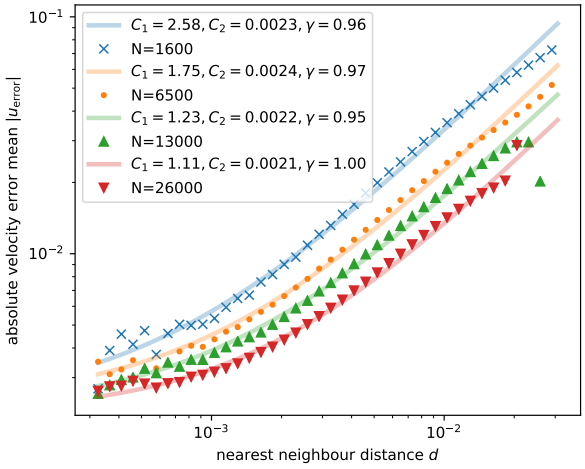

(b) Absolute velocity error of the FIT reconstructions in dependence of nearest neighbour distance d for all seeding densities. A fit of $C_1 x^\gamma + C_2$ indicates linear scaling. Only every second datapoint is displayed. The statistics at the far left and far right are not converged due to the rare occurrence of very small and very large distances.

Figure 2: **(a)** Velocity and acceleration SNR **(b)** linear scaling of the error on nearest neighbour distance.

strategy for virtual tracers based on these observations. On the one hand, the reconstruction naturally exhibits the highest errors in the absence of particles. On the other hand, the additional spatial scales are recovered in these intermediate areas.

3 Seeding of Virtual Tracers

3.1 Algorithm

The motivation for the use of additional virtual particles (VPs) instead of joint methods is the incontestable simplicity of the approach. At the same time, it can make use of the physically meaningful velocity and acceleration information that is provided by the reconstruction process and achieves a direct temporal coupling. However, one has to take care of possible noise amplification. A standard approach for this purpose is Kalman-filtering of the VP trajectories, i.e. a combination of the predicted outcome (advection) with the measurement (succeeding reconstruction). Nonetheless, this doubled the computational cost because the succeeding reconstruction would have to be performed twice, once without VPs and with VPs. Instead, VPs are davected directly forward and their weights are adjusted in the reconstruction process to prevent noise amplification. An outline of the procedure is to find in figure 1(b). Positions are drawn randomly from the subdomains to select the VPs. In the following, these are advected into the next time step by use of the velocity and acceleration data. Next, they are added to the existing particle cloud with individual weights for the updated velocity and zero weight for their initial acceleration. Based on the extended particle cloud and the weights, FlowFit reconstructs the field under the additional constraints. This way, direct temporal coupling with almost no further computational cost is achieved.

3.2 Weighting of the Virtual Particles

The advection is typically subject to relatively large errors, so it is worthwhile to deduce equations for their temporal evolution. Note, that a physically motivated estimate for the acceleration exists in the current case, so the *advection* incorporates a higher temporal derivative and is less errorneous than in the case of known initial velocity alone. However, this acceleration is uncertain (FlowFit error) and undergoes unknown continuous changes over time owing to the dynamics (dynamic error), which leads to additional errors in the estimation of the new position and velocity. Consequently, we aim to incorporate both effects into the equations by consideration of the Lagrangian statistics and the reconstruction errors. In the following, the deviation of true velocities and the reconstructed velocities (FlowFit velocity error) is denoted as ν, which reads $\boldsymbol{\nu} = \boldsymbol{u}_{\text{reconstructed}} - \boldsymbol{u}_{\text{true}}$ or $\nu = u_{\text{reconstructed}} - u_{\text{true}}$ for vectors or a single component, respectively. Analogously, for the acceleration $\boldsymbol{\alpha}$ or α is used. Because the reconstructions represent a lowpass-filtered version of the true field, the assumption of vanishing mean values of the errors ν and α is justified.

The Taylor series for a position and velocity component along a trajectory read

$$x(t) = x_0 + u_0 t + a_0 \frac{t^2}{2} + \Theta_x(t) \ , \quad u(t) = u_0 + a_0 t + \Theta_u(t). \tag{1}$$

with error terms $\Theta(t)$. In fact, the true values for u_0 and a_0 are unknown so the estimation becomes

$$x(t) = x_0 + \big(u_0 + \nu\big)t + \big(a_0 + \alpha\big)\frac{t^2}{2} + \Theta_x(t) \ , \quad u(t) = \big(u_0 + \nu\big) + \big(a_0 + \alpha\big)t + \Theta_u(t) \tag{2}$$

where the Θ's now contain the errors owing to deviations from the constant acceleration model and errors due to the reconstruction. The mean square errors (MSEs) of position and velocity become

$$\langle \Theta_x^2 \rangle = \frac{1}{4}\langle a_0^2 + \alpha^2 + 2a_0\alpha\rangle t^4 + \langle u_0 a_0 + \nu a_0 + u_0\alpha + \nu\alpha\rangle t^3 + \langle -\Delta x a_0 - \Delta x\alpha + u_0^2 + \nu^2 + 2u_0\nu\rangle t^2$$
$$-2\langle \Delta x u_0 + \Delta x\nu\rangle t + \langle \Delta x^2\rangle, \tag{3}$$
$$\langle \Theta_u^2 \rangle = \langle a_0^2 + \alpha^2 + 2a_0\alpha\rangle t^2 + 2\langle \nu a_0 + \nu\alpha - \Delta u a_0 - \Delta u\alpha\rangle t + \langle \Delta u^2 - 2\Delta u\nu + \nu^2\rangle. \tag{4}$$

Herein, the time dependent shifts $\Delta x(t) = x(t) - x_0$ and $\Delta u(t) = u(t) - u_0$ appear. Terms like $\langle \Delta x(t) u(0)\rangle$ or $\langle \Delta x(t) a(0)\rangle$ implicitly contain the Lagrangian velocity and acceleration autocovariances and crosscovariances which can be evaluated on the basis of the available particle tracks. In general, the MSEs show quite

complex dependencies but there is less reason to assume that the FlowFit errors are correlated to any of the other properties so crossterms containing ν or α are neglected. This way, equations (3) and (4) yield

$$\boxed{\langle \Theta_x^2 \rangle = \frac{1}{4}\langle a_0^2 + \alpha^2 \rangle t^4 + \langle u_0 a_0 \rangle t^3 + \langle u_0^2 + \nu^2 - \Delta x a_0 \rangle t^2 - 2\langle \Delta x u_0 \rangle t + \langle \Delta x^2 \rangle} \tag{5}$$

$$\boxed{\langle \Theta_u^2 \rangle = \langle a_0^2 + \alpha^2 \rangle t^2 - 2\langle \Delta u a_0 \rangle t + \langle \Delta u^2 + \nu^2 \rangle,} \tag{6}$$

All of the terms can be evaluated and binned spatially by use of (i) the particle track data and (ii) benchmarking in order to estimate the reconstruction errors. In the testcases the reconstruction error could be accessed directly. This way, spatial variations of the dynamic time scales and the reconstruction errors are covered. To apply the results for a weighting of virtual particles, the considerations have to be generalized to three dimensions. Because FlowFit does not consider a positional error, the MSE in position must be added to the velocity error by consideration of the estimated velocity gradients, so

$$\sigma_u^2 = \langle \tilde{\Theta}_u^2 \rangle \approx \langle \Theta_u^2 \rangle + C_{\text{gradient}} \begin{pmatrix} \left(\frac{\partial u}{\partial x}\right)^2 \\ \left(\frac{\partial u}{\partial y}\right)^2 \\ \left(\frac{\partial u}{\partial z}\right)^2 \end{pmatrix} \cdot \begin{pmatrix} \langle \Theta_x^2 \rangle \\ \langle \Theta_y^2 \rangle \\ \langle \Theta_z^2 \rangle \end{pmatrix}, \tag{7}$$

and analogously for the velocity components v and w. C_{gradient} is a constant greater than 1, which accounts for the smoothening of gradients in the reconstruction. With these errors at hand, a weighting function for the virtual particles can be introduced like

$$\text{velocity weight} = \frac{\text{rmse of tracked velocities}}{\text{rmse of virtual particle velocities}} = \frac{\text{rmse of tracked velocities}}{\sqrt{(\sigma_u^2 + \sigma_v^2 + \sigma_w^2)/3}} \approx \frac{C_{\text{weight}}}{C_{\text{weight}} + \sqrt{(\sigma_u^2 + \sigma_v^2 + \sigma_w^2)/3}}, \tag{8}$$

which takes values smaller 1 to account for the lower reliablity of the virtual particles. Here, another constant C_{weight} was introduced, because the tracked velocities in the testcases have no quantifiable error.

4 Results

4.1 Influence of Virtual Particles

In this section, the effect of additional VPs on the reconstruction quality is analysed. One aims to minimize the error over time and so the total MSEs, i.e. MSEs averaged over the subdomains, serve as comparison criterion. The temporal evolution of the total MSEs under influence of VPs are presented in figures 3(a) and 3(b) for the FIT und CF testcase, respectively. The graphs show that the velocity MSE decreases rapidly within the first 10 time steps and the very first step even causes a great drop in the FIT testcase. Thereafter, the velocity MSE ratio levels at values between 0.9 and 0.7 corresponding to an mean square error reduction of 10% to 30%. Only velocity data is given at the VP positions, but still the acceleration MSE decreases and levels accordingly. The gain in acceleration reaches from 0% to 15%. Note, that the graphs display the temporal evolution of the total MSEs of single realisations in rather small subdomains. Therefore, the graphs appear rather noisy and show some abrupt changes whenever badly resolved structures leave or enter the domain. Moreover, the MSE values to which the graphs are normalized differ greatly due to the higher accuracy in the case of high seeding densities. For this reason, the noisy appearance of the acceleration a_x in the highly seeded channel flow testcase should be interpreted with care.

In summary, simultaneous MSE reductions of up to 30% for velocity and 15% for acceleration were achieved by the seeding of VPs. Anyhow, the instant MSE drop of 15% to 17% clearly is contradictive because two timesteps are only seperated by $\tau_\eta/4$ and the initial particle cloud is not expected to show high relative shifts. Thus, two successive timesteps contain basically the same information and there is simply no physical reason for an instant error drop of this size. This drop could theoretically depend on the transport of good information into the boundary where the reconstruction is known to yield significantly higher errors. However, this effect was already accounted for by excluding the boundary from the MSE calculation itself, so it cannot be the cause of this considerable gain.

Regardless of cause, the effect is present. So one could try to exploit it further and cumulate the effect by successive forward and backward propagation of VPs between two timesteps. This is rendered reasonable because the dissipation is practically neglectable on Kolmogorov time scales and the Euler equations are time reversible. Interestingly, it is not possible to reach a higher gain. Quite the opposite is the case, the MSEs grow during a backward step and decrease again during a forward step. Several trials yield the very same qualitative results. This observation enforces that the erroneous boundary is not the cause for the enhancement. Additionally, one can deduce that at least a part of the effect is not directly physical but rather a product of the reconstruction process. In order to rule out the mechanisms behind the instant enhancement, it is necessary to reconsider equation (4). It is already known, that during the advection process the velocity MSE changes according to equation (4). Therein, the shift Δu can be approximately expressed by $a_0 t$. This yields the neat and compact equation

$$\langle \Theta_u^2 \rangle = \langle \nu^2 \rangle + \langle \alpha^2 \rangle t^2 + 2\langle \nu\alpha \rangle t. \tag{9}$$

Therein, all but the last term have positive sign by definition. If the last term is non-vanishing and negative, the velocity MSE will initially decrease for small positive timesteps until the quadratic term takes over. For negative time shifts, all terms will be positive and no such effect can occur. Indeed, when the reconstructions are checked for the a priori neglected term, the average correlation coefficients $C_{\nu\alpha} = \langle \nu\alpha \rangle (\langle \nu^2 \rangle \langle \alpha^2 \rangle)^{-1/2}$ in tables 2 and 3 are found. They take absolute values between circa 0.07 and 0.45 and grow with the number of seeded particles. Equation (9) suggests that the possible gain will depend on the strength of this correlation and the time shift. The maximum MSE reduction is to find at the minimum of the parabola (9). It occurs at t^* and causes a relative gain of $C_{\nu\alpha}^2$ because

$$t^* = -\frac{\langle \nu\alpha \rangle}{\langle \alpha^2 \rangle} = -C_{\nu\alpha} \sqrt{\frac{\langle \nu^2 \rangle}{\langle \alpha^2 \rangle}} \quad \Rightarrow \quad \frac{\langle \Theta_u^2 \rangle^*}{\langle \nu^2 \rangle} = 1 - C_{\nu\alpha}^2 \ \in [0,1] \tag{10}$$

By pure chance, the initially chosen frame spacings in table 1 coincide almost perfectly with the optimal timesteps t^* for both testcases. Thus, the effect predicts maximum enhancements between 0.6% and 20% dependent on the seeding density. Consequently, it explains the instant error reduction in the highly seeded FIT cases and the error amplification during backwards advection. But the error-correlation model fails to capture the total gain in the other cases, which suggests that the temporal coupling performs like intended.

A before and after comparison of a flow field is presented in figure 4. The vortical structures remain mostly unchanged but some are elongated and/or reconnected so they appear less 'blobby'. A visualization of the gain reveals that it partly coincides with the presence of prominent vortical structures in this example and enforces the hypothesis, that spatial scales - once resolved - persist longer under influence of virtual tracers.

Table 2: Velocity and acceleration error correlation coefficients for several particle densities in FIT.

#particles	$C_{\nu\alpha}$		
	x-component	y-component	z-component
1600	-0.156	-0.183	-0.135
6500	-0.238	-0.260	-0.218
13000	-0.321	-0.352	-0.308
26000	-0.432	-0.458	-0.419

Table 3: Velocity and acceleration error correlation coefficients for several particle densities in CF.

#particles	$C_{\nu\alpha}$		
	x-component	y-component	z-component
2000	-0.233	-0.078	-0.147
8400	-0.335	-0.166	-0.226
16400	-0.37	-0.22	-0.287

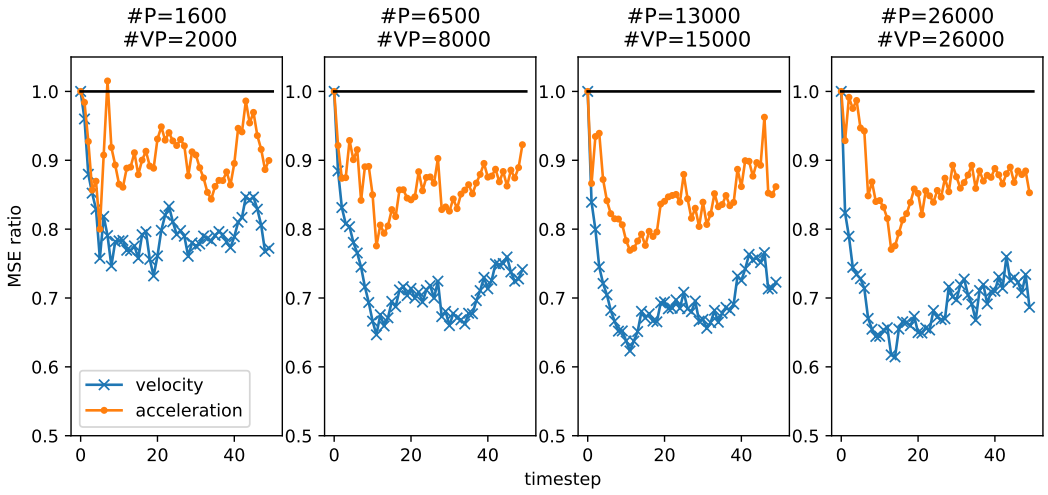

(a) Forced isotropic turbulence testcase

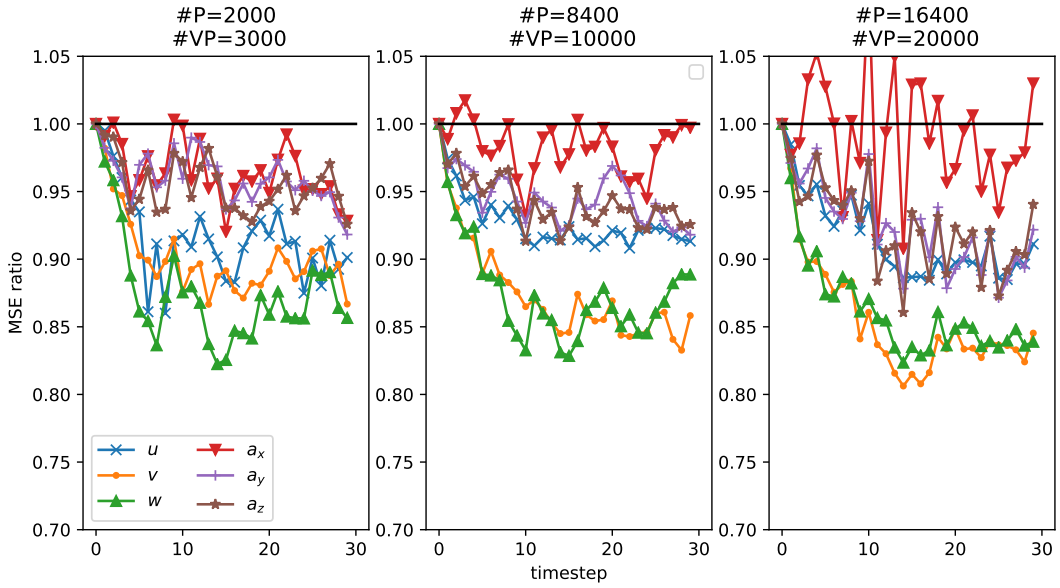

(b) Channel flow testcase

Figure 3: Ratio of the velocity and acceleration MSEs of reconstructions including and not including virtual particles dependent on time. The black line displays the normalized MSE of the initial reconstruction containing only #P true particles so a value smaller than 1 indicates an enhancement. The procedure resulted in a considerable decrease of the total MSEs for all seeding densities in both testcases. The relative weight of the VP velocities in FlowFits costfunction was set to approximately 0.7 by adjusting the parameters C_{gradient} and C_{weight}.

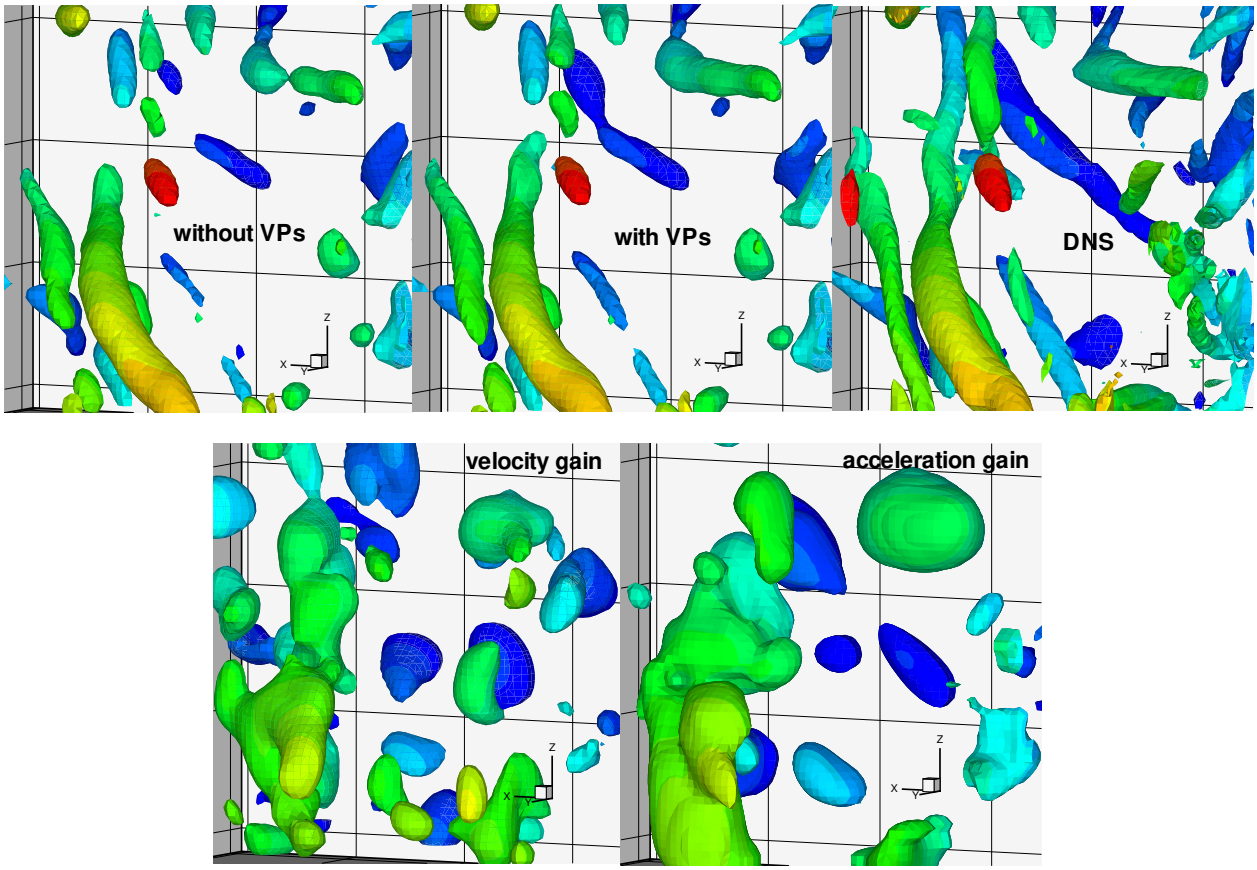

Figure 4: **Top row:** Q-isosurface of the FIT flow field at timestep 34 for reconstructions without VPs, with VPs and the DNS. #particles = 1600. The vortical structures appear clearly elongated and/or reconnected after the seeding of virtual particles. Surfaces are color coded by y-coordinate. **Bottom row:** Isosurfaces of spatially smoothened velocity and acceleration gain. Surfaces are color coded by y-coordinate. The gain is found near the prominent vortical structures. Statistics reveal that the mean gain is highest in regions with high Q-absolute, including both, foci and nodes.

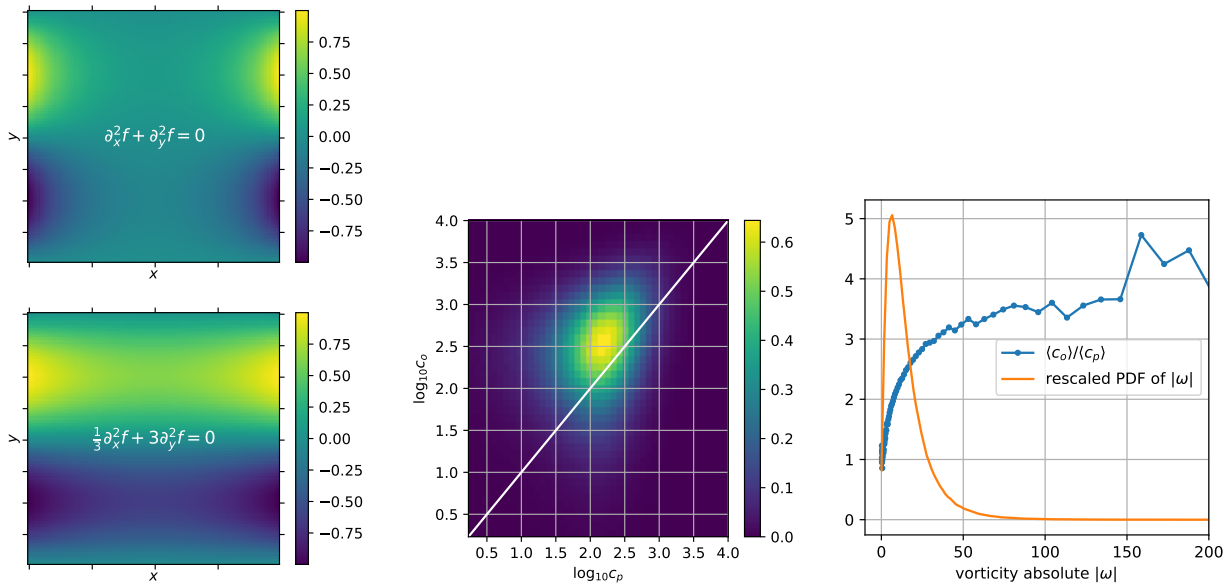

(a) Solutions to the isotropic and an anisotropic 2D Laplace equation in a square domain with a single sine wave $\sin(2\pi x/L)$ as boundary condition at $y = 0$ and $y = L$.

(b) Joint PDF of velocity curvature orthogonal and parallel to the vorticity. The white line marks $c_0 = c_p$. The curvature orthogonal to vorticity direction is significantly higher.

(c) Rescaled PDF of the vorticity (orange) and the ratio of mean orthogonal and mean parallel curvature binned for vorticity absolute. The ratio increases rapidly in the presence of swirling motion.

Figure 5: Regarding the potential gain of anisotropic curvature penalization.

4.2 Anisotropic Curvature Penalization for Vortex Elongation

FlowFit relies on a regularization (curvature penalization) to make the underdetermined inverse problem uniquely solvable. So the regularization is not physically motivated but a pure necessity. In the previous section, a flow field that shows unconnected vortex blobs owing to missing particle data in the intermediate zones was presented. These gaps are reduced partly by use of virtual particles. Basically, it would be desirable to make the regularization itself favour vortex tubes instead because these are more common structures: The teardrop shape of the joint PDF of velocity gradient tensor invariants Q and R reveals that vortical motion is more likely to appear in the form of stable foci together with a stretching motion. Vorticity itself is accordingly distributed in a prolate fashion owing to the self-stretching term. So, the vortex dynamics induce local anisotropy such that, e.g., spatial derivatives like the curvature of the velocity fields are smaller in the direction of vorticity.

To base the idea on solid ground, the Hessian $\mathbf{H}$ of the velocity fields in the FIT testcase is evaluated by use of the provided analysis tools. The curvature of a velocity field along the direction of vorticity $\boldsymbol{n}_\parallel = \boldsymbol{\omega}|\boldsymbol{\omega}|^{-1}$ is expressed by $c_p = |\boldsymbol{n}_\parallel^\intercal \mathbf{H} \boldsymbol{n}_\parallel|$, which will be called parallel curvature in the following. Analogously, the orthogonal curvature reads $c_o = |\boldsymbol{n}_\perp^\intercal \mathbf{H} \boldsymbol{n}_\perp|$ with $\boldsymbol{n}_\perp \cdot \boldsymbol{n}_\parallel = 0$. Indeed, the mean values of both curvature absolutes are comparable in the absence of swirling motion, compare figure 5(c), but their ratio increases rapidly with vorticity. Consequently, an initial estimate of the vorticity field can be translated into an advantageous regularization.

Figure 5(a) illustrates the difference of isotropic and anisotropic curvature penalization on a toy model. If the sinusoidal boundary condition is interpreted as a cut through a vortex profile, one observes that the profile will be less dampened inside the square domain under anisotropic curvature penalization. A similar effect can potentially lengthen vortical structures within FlowFits reconstruction process and lessen the gaps between single vortex blobs - yet it needs to be implemented.

5 Conclusion

The very simple but successful approach of virtual tracers resulted in total mean square velocity error reductions between 10% and 30% in two independent virtual experiments. This was achieved with almost no further computational cost, although the temporal distance between the reconstructions was set rather conservative in the present cases. The acceleration behaved accordingly, but the total gain was smaller. In parts, the velocity enhancement was overshadowed by spurious correlations between velocity and acceleration errors which acted advantageously on the total mean square error. The question for the origin of these correlations remains open, although they can either be caused by the reconstruction process itself or be a result of the local interpolation schemes in the Johns Hopkins Turbulence Database that do not satisfy solenoidality. However, the influence of these correlations did not suffice to capture the full size of the error reductions. This way, the advantageous influence of virtual particles can be traced back to the fulfillment of the additional temporal coupling. Eventually, the hypothesis that virtual particles can enforce temporal consistency and conserve the structures beyond Nyquist is confirmed to some extent. Noise amplification was no problem in the present cases owing to mild densities of virtual tracers and their reduced weighting inside FlowFits cost function.

References

Christiansen I (1973) Numerical simulation of hydrodynamics by the method of point vortices. *Journal of Computational Physics* 13:363–379

Gesemann S, Huhn F, Schanz D, and Schröder A (2016) From Noisy Particle Tracks to Velocity, Acceleration and Pressure Fields using B-splines and Penalties. in *18th International Symposium on Applications of Laser Techniques to Fluid Mechanics, Lisbon, Portugal, July 4–7*

Graham J, Kanov K, Yang X, Lee M, Malaya N, Lalescu C, Burns R, Eyink G, Szalay A, D Moser R, and Meneveau C (2016) A Web services accessible database of turbulent channel flow and its use for testing a new integral wall model for LES. *Journal of Turbulence* 17:181–215

Li Y, Perlman E, Wan M, Yang Y, Meneveau C, Burns R, Chen S, Szalay A, and Eyink G (2008) A public turbulence database cluster and applications to study Lagrangian evolution of velocity increments in turbulence. *Journal of Turbulence* 9:N31

Schanz D, Gesemann S, and Schröder A (2016) Shake-The-Box: Lagrangian particle tracking at high particle image densities. *Experiments in Fluids* 57:70

Schneiders J, Azijli I, Scarano F, and Dwight R (2015) Pouring time into space. in *11th International Symposium on Particle Image Velocimetry - PIV15, Santa Barbara, CA, USA, September 14-16*

Schneiders J and Scarano F (2018) On the use of full particle trajectories and vorticity transport for dense velocity field reconstruction. in *19th international Symposium on Application of Laser and Imaging Techniques to Fluid Mechanics - LXLASER2018, Lisbon, Portugal, July 16-19*

Schröder A, Geisler R, Staack K, Elsinga GE, Scarano F, Wieneke B, Henning A, Poelma C, and Westerweel J (2011) Eulerian and Lagrangian views of a turbulent boundary layer flow using time-resolved tomographic PIV. *Experiments in Fluids* 50:1071–1091

Yu H, Kanov K, Perlman E, Graham J, Frederix E, Burns R, Szalay A, Eyink G, and Meneveau C (2012) Studying Lagrangian dynamics of turbulence using on-demand fluid particle tracking in a public turbulence database. *Journal of Turbulence* 13:N12